Architecture-Dependent Stability, Cellular Uptake, and Redox Modulation of Poly(p-Coumaric Acid) Hybrid Nanoparticles for Ovarian Carcinoma Intervention

M. Megahed,[1,+] A. Harun,[1,3,+] K. Herrera,[1,2+] Md. H. Rashid,[1] I. De Leon,[1] I. Srivastava[1,3,]*

[1] Department of Mechanical Engineering, Edward E. Whitacre Jr. College of Engineering, Texas Tech University, Lubbock, Texas 79409, United States

[2] Department of Biology, Texas Tech University, Lubbock, Texas 79409, United States

[3] Texas Center for Comparative Cancer Research (TC3R), Amarillo, Texas, 79106, United States

[+] denotes co-first author

** Authors to whom correspondence should be addressed: indrajit.srivastava@ttu.edu*

KEYWORDS. Polycondensation, Macromolecular Architecture, Self-Therapeutic Polymers, Structure-Property Relationships, NIR-I Fluorescence, 3D Bioprinting

ABSTRACT. The clinical efficacy of fluorescence-guided surgery (FGS) is often compromised by the poor photostability and biologically inert nature of conventional contrast agents like Indocyanine Green (ICG). While nanocarriers can enhance dye stability, they typically function as passive delivery vehicles, requiring additive complexity to achieve therapeutic effects. Here, we report a structure-guided approach to develop self-theranostic hybrid nanoparticles where the polycondensation kinetics of the polymer core, poly(p-coumaric acid) (PCA), serve as a master switch for both optical and biological performance. By systematically tuning the reaction duration, we synthesized PCA variants with distinct macromolecular growth profiles that dictate the efficiency of nanoparticle assembly and hydrophobic sequestration. Optimized PCA architectures significantly enhanced the photostability of encapsulated ICG *via* nanoprecipitation, maintaining robust NIR-I fluorescence under continuous surgical illumination. Beyond acting as a structural scaffold, the PCA matrix retains intrinsic redox activity, triggering apoptosis in ovarian cancer cells *via* the modulation of reactive oxygen species (ROS) generation. The translational utility of these nanoparticles was validated using 3D bioprinted intraperitoneal tumor phantoms, which recapitulate the optical scattering and spatial heterogeneity of metastatic disease to enable high-contrast surgical simulations. This work establishes reaction-time-dependent architecture as a critical design parameter for integrating imaging and intrinsic therapeutic functionalities within a single, simplified nanomaterial platform.

INTRODUCTION.

Fluorescence-guided surgery (FGS) has emerged as a transformative modality for enhancing surgical precision, enabling real-time, high-contrast visualization of malignant margins.[1, 2] Among clinically approved fluorophores, Indocyanine Green (ICG) remains the gold standard due to its near-infrared (NIR-I) emission and deep tissue penetration.[3, 4] However, the translational utility of free ICG is severely hampered by rapid photobleaching, concentration-dependent quenching, and poor aqueous stability.[4, 5] These limitations lead to premature signal decay during prolonged cytoreductive procedures, often necessitating repeated dosing or compromising the detection of residual micro-tumors.[6-8]

To mitigate these drawbacks, diverse nanocarrier platforms have been engineered to encapsulate and stabilize ICG.[8, 9] While successful in improving optical longevity, most existing systems are designed as biologically inert "shipping containers" that contribute no therapeutic value.[8, 10] This stark dichotomy between imaging functionality and therapeutic efficacy represents a missed opportunity in nanomedicine design, where multifunctionality is typically achieved through "additive complexity", the conjugation of multiple disparate components, rather than the intrinsic material properties of the scaffold itself.[11, 12]

An elegant solution lies in the development of self-therapeutic polymers, where the macromolecular backbone possesses innate biological activity.[13, 14] Bio-derived phenolic polymers are particularly compelling candidates due to their inherent redox activity and ability to modulate intracellular oxidative stress.[15,16] Poly(p-coumaric acid) (PCA), synthesized via the polycondensation of naturally occurring p-coumaric acid, represents a unique class of "active"

scaffolds.[13,17] Despite the potential of such systems, a fundamental gap remains: the role of macromolecular architecture in governing the transition from a chemical scaffold to a functional nanomedicine. In current literature, polymer structure is frequently treated as a fixed attribute rather than a tunable design variable.[13,18] Consequently, the correlation between polymerization kinetics, nanoparticle assembly, and emergent theranostic performance remains largely unexplored.[12,19]

Here, we demonstrate that the polycondensation kinetics of PCA serve as a 'master switch' for nanoparticle performance in ovarian carcinoma models. By systematically tuning the reaction duration, we synthesized PCA variants with distinct macromolecular growth profiles that dictate the efficiency of hybrid lipid–polymer assembly. We show that allowing for extended polymer growth facilitates superior hydrophobic sequestration of ICG, providing unprecedented photostability under continuous surgical illumination. Furthermore, we demonstrate that this kinetic control extends to the biological interface; nanoparticles formulated from optimized reaction times exhibit enhanced cellular uptake and trigger apoptosis by modulating reactive oxygen species (ROS) generation. Finally, to bridge the gap toward clinical implementation, we validate these nanoprobes using 3D bioprinted intraperitoneal tumor phantoms that recapitulate the optical scattering and spatial heterogeneity of metastatic disease. This work establishes reaction-time-dependent architecture as a critical design parameter for the rational engineering of next-generation, structure-guided nanomedicines.

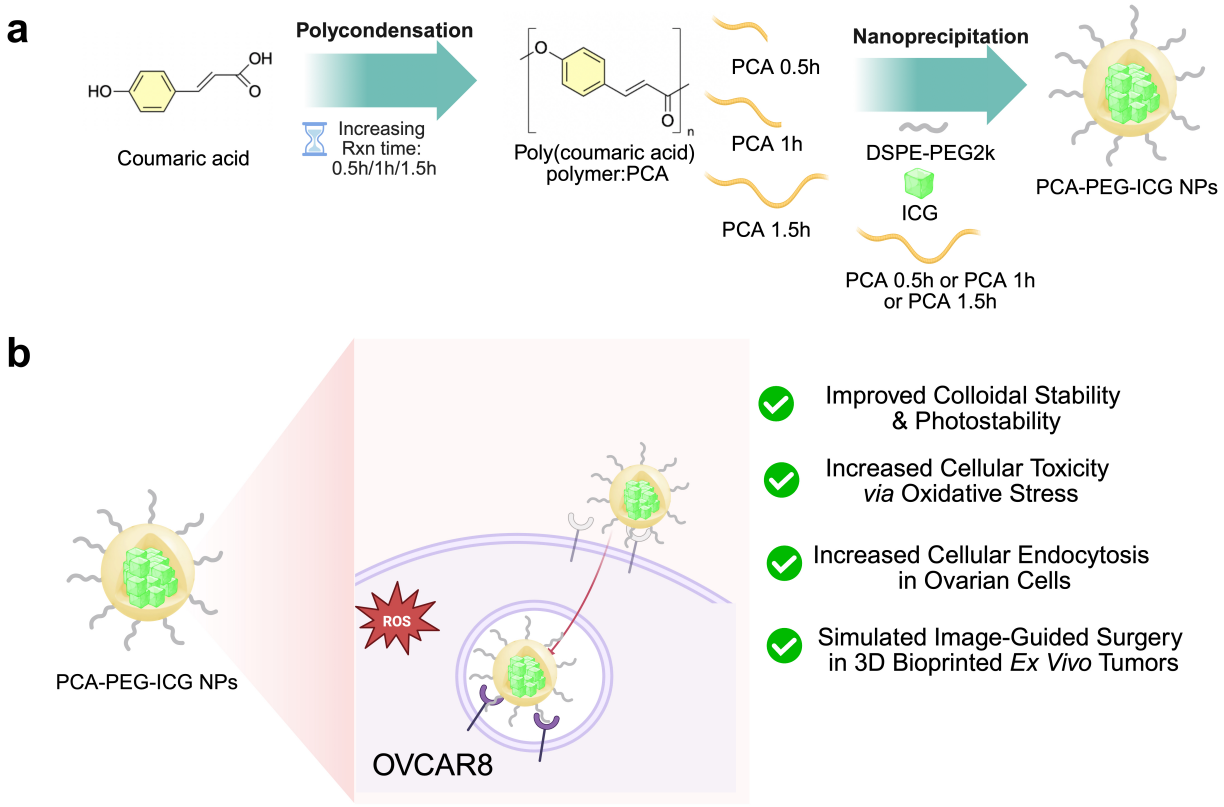

Figure 1. Schematic illustration of the synthesis, formulation, and biological evaluation of PCA-PEG-ICG nanoparticles. (a) Coumaric acid undergoes polycondensation to form poly(coumaric acid) (PCA) with varying reaction times (0.5, 1, and 1.5 h). The resulting PCA polymers are then formulated into nanoparticles via nanoprecipitation with DSPE-PEG2k and ICG, yielding PCA-PEG-ICG NPs. (b) The nanoparticles exhibit increased cellular uptake via endocytosis, and elevated cytotoxicity mediated by oxidative stress in OVCAR8 cells. Additionally, the NPs showed enhanced colloidal stability and photostability and are evaluated in *ex vivo* bioprinted tumor models to simulate image-guided surgery (IGS) applications.

MATERIALS AND METHODS.

Materials. All materials were purchased from Sigma-Aldrich and used without modification, unless otherwise stated. Porcine skin tissue was obtained from local grocery stores. Preserved bovine brains with dura mater, porcine ovaries, and dry-preserved porcine lung tissue were purchased from Nasco Education.

Preparation and Characterization of Poly-Coumaric acid (PCA). Poly coumaric acid was synthesized using polycondensation reaction at three different reaction times. Under 4°C ice bath conditions, 10 ml of anhydrous pyridine was stirred for 5 min in a round bottom flask, followed by the addition of 5 mmol of thionyl chloride. After 15 min the round bottom flask was removed from the ice bath, and 2.5 mmol of p-coumaric acid was added and left to stir at room temperature for 30 min, 1 hour and 1.5 hours (referred as PCA0.5h, PCA1h, and PCA1.5h respectively). 1% HCL was then added to stop the reaction, and the samples were washed twice (13000 rpm, 30 mins) using Ultrapure water and then lyophilized into powders. 1H-NMR spectroscopy was used to characterize the polymers' structures and composition using a 400 MHz spectrometer. Ultraviolet-visible (UV-VIS) absorption was recorded using the Genesys 30 Visible Spectrophotometer (ThermoFisher Scientific).

Preparation and Characterization of Poly-Coumaric Acid Nanoparticles (PCA-PEG NPs). Following the synthesis of poly-coumaric acid (PCA) at reaction times of 0.5 h, 1 h, and 1.5 h, the polymers were used to formulate NPs using DSPE-PEG *via* nanoprecipitation [20-22]. The aqueous phase was identical for all reaction times and consisted of 8 mL of PBS 1X. The organic phase of the PCA-PEG NPs consisted of 1 mL of the PCA stock solution (1 mg/mL in DMSO), 1 mL of

DMSO and 500 μL of the DSPE-PEG stock solution (1 mg/mL in DMSO). For PCA-PEG-ICG NPs, the organic phase consisted of 1 mL of the PCA stock solution, 500 μL of the DSPE-PEG stock solution, 500 μL of DMSO, and 200 μL of ICG stock solution (1 mM in DMSO). The organic phase was added dropwise to the aqueous phase while sonicating. Upon completion, the NPs were ultracentrifuged at 4,500 rpm for 10 min and washed four times with PBS 1X to remove unreacted precursors and free ICG. The washed NPs were then filtered through a 0.22-μm PVDF filter and stored at 4 °C.

Physicochemical and Optical Characterization of PCA-PEG and PCA-PEG-ICG NPs. Hydrodynamic diameter (HD) and polydispersity index (PDI) were determined via dynamic light scattering (DLS), using the Litesizer DLS 700 Particle Analyzer instrument (Anton Paar). ζ-potential measurements also used the Litesizer DLS 700 Particle Analyzer. Ultraviolet-visible (UV-VIS) absorption was recorded using the Genesys 30 Visible Spectrophotometer (ThermoFisher Scientific). All absorbance measurements were recorded with scanning intervals of 2 nm from 250 to 1100 nm. Fluorescence characterization of PCA-PEG-ICG NPs was performed using a fluorescence spectrophotometer RF6000 (Shimadzu) at an excitation wavelength of 785 nm and an emission range of 800–900 nm.

Transmission Electron Microscopy Imaging (TEM). Carbon coated copper grids of 200 mesh were glow discharged immediately prior to use to render the surface hydrophilic. A drop of PCA NP was then applied to the grid surface, and it was incubated for 60 seconds. Excess liquid was removed by blotting with filter paper. Negative staining was performed by adding a drop of freshly prepared 1% w/v uranyl acetate solution to the grid surface, followed by a 30-second incubation.

Excess stain was then carefully blotted away, and the grids were dried under vacuum at room temperature overnight. All samples were imaged using a Hitachi H-7650 transmission electron microscope at 100 kV.

PCA NPs Stability Assessment. The colloidal stability of the PCA1.5-PEG5, PCA1.5-PEG5-ICG, PCA1-PEG5-ICG and PCA0.5-PEG5-ICG NPs was evaluated by incubating them with PBS buffer 1x (pH 7.4) at 4°C and 37°C and with 1% plasma at 37°C. The size stability was tested by DLS over 7 days.

Cytotoxicity Evaluation *In Vitro*. The cytotoxic effects of PCA0.5h-PEG5, PCA1h-PEG5 and PCA1.5h-PEG5 were assessed using the colorimetric MTT assay. OVCAR8 cells, a human ovarian carcinoma cell, (5×10^4 cells/well) were seeded in 96-well plates in 200 µL of Reconstituted DMEM medium for 24 h and then cultured with NPs at increasing concentrations (1, 5, 10, 25, 50, and 100 µg/mL) for 48 h. Subsequently, cells were incubated with 10 µL of MTT stock solution in PBS (0.5 mg/mL)/well for 4 h, followed by dissolving the formazan crystals with 200 µL of DMSO. The absorbance was measured using the BioTek Epoch 2 Microplate Spectrophotometer (Agilent) at 592 nm.

***In Vitro* Cellular Uptake of PCA1.5-PEG5-ICG NPs**. As PCA1.5-PEG5-ICG NPs showed an optimized architectural and stability design, their cellular internalization was first assessed. OVCAR8 cancer cells were seeded in 6-well plates at a density of 2×10^5 cells per well and cultured in DMEM supplemented with 10% fetal bovine serum (FBS). After 24 hours, the cells were incubated with PCA1.5-PEG-ICG NPs for 4, 8, 12and 24 h at an ICG concentration of 7.5 µM. Following incubation, cells were collected into microcentrifuge tubes, and the fluorescence

emission images were then measured using an IVIS imaging system at an excitation filter of 745 nm and an emission filter of 840 nm.

***In Vitro* Cellular Uptake of PCA0.5-PEG5-ICG NPs and PCA1-PEG5-ICG NPs.** OVCAR8 cancer cells were seeded in 6-well plates at a density of 2×10^5 cells per well and cultured in DMEM supplemented with 10% fetal bovine serum (FBS). As the optimal cellular intake was observed at 24 h with using PCA1.5-PEG5-ICG NPs, the cells were incubated with PCA0.5-PEG5-ICG and PCA1-PEG5-ICG NPs for 24 h at an ICG concentration of 7.5 μM. Following incubation, cells were collected into microcentrifuge tubes, and the fluorescence emission images were then measured using an IVIS imaging system at an excitation filter of 745 nm and an emission filter of 840 nm.

Encapsulation Efficiency of PCA-PEG5-ICG NPs. The encapsulation efficiency (EE) of ICG using PCA1.5-PEG5-ICG, PCA1-PEG5-ICG and PCA0.5-PEG5-ICG was assessed using UV–Vis spectroscopy using the Genesys 30 Visible Spectrophotometer (ThermoFisher Scientific) at an absorption of 702 nm. A calibration curve was prepared using ICG diluted with DMSO at increasing concentrations (0.1-100 μM). The absorption spectrum of the NPs was then collected under the same conditions and ICG content was then quantified based on the calibration curve.

The encapsulation efficiency was calculated according to the following equation:

$$EE\% = \left(\frac{Concentration\ of\ encapsulated\ ICG}{Concentration\ of\ Added\ ICG}\right) \times 100$$

Tumor Mimicking Phantom Stock Solution Preparation. A tumor mimicking phantom stock solution was made by combining 17 mL of PBS 1X, 900 µL of intralipid 20%, 150 mg of porcine hemoglobin, and 720 mg of type-A gelatin. The gelatin was activated following a continuous stirring at 65°C and 950 rpm for at least 30 minutes until the gelatin is fully dissolved in PBS1X. After activation, intralipid and hemoglobin were added to the solution and the mixture was inverted and vortexed, it was further mixed for 10 minutes at 950 rpm at 65°C. The stock was further used to synthesize different compositions of phantom with PCA-PEG NPs and PCA-ICG-PEG NPs.

Quantitative Fluorescence Imaging using PCA-PEG-ICG Tumor-Mimicking Phantoms. 1.5mL phantom stock solution was added with 0.5mL PCA1.5h-PEG5-ICG NP using a two-fold serial dilution of the NP with an initial concentration of 10 µM in silicon mold wells. The phantoms were solidified in the freezer at -20°C overnight. A control phantom was made using 2mL of phantom stock solution only in the silicon mold well following solidification in the freezer. The IVIS image of the phantoms were collected placing them in a well plate using the IVIS imaging system at the excitation wavelength of 745 nm and emission wavelength of 840 nm.

***Ex Vivo* Porcine Tissue Penetration Profiling.** Three different porcine tissue samples were used to simulate the characteristics of human skin, muscle, and fat tissues. A piece of pork belly was used to replicate skin tissue, pork tenderloin was used to resemble muscle tissues, and a fatty pork chop was used as fat tissue. Using a deli meat slicer in the lab, all tissues were consistently sliced to a thickness of 2 mm after being obtained from nearby supermarkets. The tissue slices were stacked in accordance with the variation in tumor depth in a well plate covering the PCA1.5h-PEG5-ICG NP phantom made with 1.5mL of phantom stock solution and 0.5mL of PCA1.5h-PEG5-ICG NP solution. The same tissue stacking simulation was performed in an ICG phantom made with 1.5mL of phantom stock solution and 0.5mL of ICG solution of 10 µM. From surface-

level to deep tumor lesions, tissues were stacked at different depths from 0 mm to 4 mm where cancers can develop. Fluorescence images were acquired using an IVIS imager at 745 nm excitation and 840 nm emission filter.

Photobleaching Assessment of PCA-ICG NP. PCA1.5hr_PEG5_ICG NP TMP, ICG TMP and Control TMPs were made following the methods described above. The TMPs were placed in a well plate and exposed to a 1000 lumen white light source for different time periods (1min, 0.5h, 2h, 4h). Fluorescence images were collected at each time point after being exposed to the white light source using an IVIS imager at 745 nm excitation and 840 nm emission window.

3D Bioprinting of Intraperitoneal Tumors. To create the intraperitoneal tumors, skin' mimicking phantoms were printed, and TMPs with nanoparticles were printed on top of 'skin' mimics. The skin mimics were printed using 500 μL of melanin solution (2mg/mL) mixed with 2 ml of high concentration gelatin solution (6%). The mixture was placed in a syringe and added into the printer. By setting specific printing parameters and freezing the mixture to 2°C the skin mimicking phantom was printed. To print the small Tumor Mimicking Phantoms on top of the 'skin' mimic, the printing parameters were kept similar except the dimensioning had been decreased to 1mmx1mm to 0.1mmx0.1mm. 1.5 mL of the Tumor Mimicking Phantom solution was mixed with 500 μL of PCA1.5h-PEG5-ICG NPs, then added to a syringe and printed. By changing the translations on the x, y, and z axis of the printer, separate small tumor phantoms at multiple desired locations were printed on top of the skin print.

RESULTS AND DISCUSSION.

Synthesis and Characterization of Poly(Coumaric Acid) at Different Reaction Times. PCA was synthesized through a one-step polycondensation reaction of CA, using thionyl chloride as an activating agent in pyridine. Pyridine acted as both the solvent and base to facilitate the polycondensation reaction.[14, 16, 23] We aimed to demonstrate that the duration of the polycondensation reaction influences polymeric nature of PCA and, consequently, its physicochemical and antioxidant properties after nanoparticles (NPs) formation **(Figure 2a)**. UV-Vis absorbance spectroscopy was used to evaluate the structural changes associated with PCA polymerization at different reaction times. As shown in **Figure 2 b,c,** the spectra of free CA and PCA samples were compared. Free CA displayed a maximum absorbance peak at 314 nm, whereas PCA 0.5h, PCA1h, and PCA1.5h showed absorbance maxima at 316, 318, and 320 nm, respectively. The progressive red shift observed with increasing reaction time suggests an increase in conjugation length, indicative of a greater extent of polymerization. Notably, PCA1.5h exhibited the most pronounced shift, consistent with more extended π-conjugation along the polymer backbone.[24] ^{1}H-NMR spectroscopy further confirmed successful polymer formation. Free CA showed a characteristic downfield singlet for the carboxylic acid proton (-COOH) at ~10-12 ppm and a broad phenolic OH signal at ~9-10 ppm. In contrast, the disappearance of the carboxylic acid signal PCA **(Figure 2 d,e and Figure S2-S5)** indicates that these groups participated in the polycondensation reaction, forming ester linkages along the backbone **(Figure S1)**. [13, 14, 17] Additionally, spectra in **Figure S3-S5** show progressively sharper signals corresponding to the alkene protons, suggesting increased structural regularity and a more defined polymer backbone with longer reaction times.

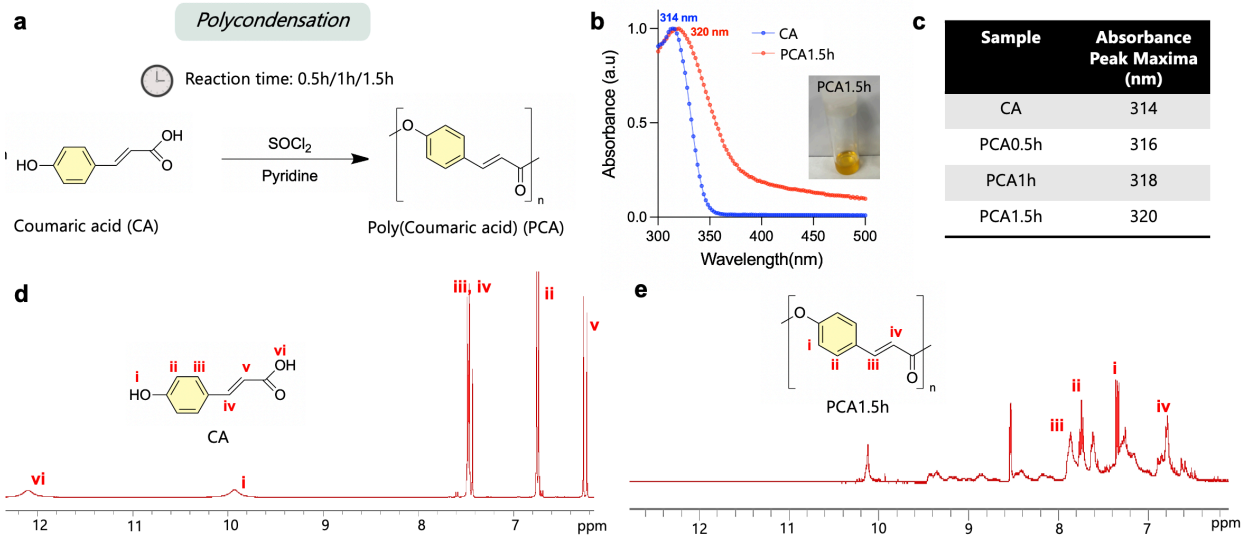

Figure 2. Time-dependent polycondensation reaction to synthesize poly(coumaric acid) and their characterization. (a) Schematic overview of poly-coumaric acid (PCA) synthesis through one step poly condensation using coumaric acid (CA) (b) UV-Vis absorbance spectra of coumaric acid (CA) and PCA 1.5h polymer (c) UV-Vis-NIR absorbance spectra of CA and PCA at various reaction times (d, e) 1H-NMR spectroscopy of CA and PCA1.5h showing the disappearance of the carboxylic group peak at 12 ppm as the polymer is formed.

Synthesis and Physicochemical Characterization of PCA-PEG Nanoparticles. PCA is a phenolic polymer derived from coumaric acid, a naturally occurring hydroxycinnamic acid found in fruits and vegetables such as tomatoes.[13, 25] In this study, PCA was co-assembled with DSPE-PEG during nanoprecipitation to form hybrid nanoparticles (NPs). DSPE-PEG, an amphiphilic polymer-lipid conjugate, facilitates NPs formation while providing steric stabilization and improves colloidal stability in aqueous media **(Figure 3a)**.[26, 27] To assess the effect of polymer

structure on NPs formation, transmission electron microscopy (TEM) was performed on PCA-PEG NPs prepared from PCA polymers synthesized at different reaction times (0.5 h, 1 h, and 1.5 h), using fixed DSPE-PEG concentrations (5mg/mL). PCA0.5-PEG5 NPs exhibited irregular aggregation and poorly defined structures **(Figure 3c, S7)**. In contrast, PCA1-PEG5 NPs showed improved structural organization, with the emergence of a more distinct core **(Figure 3c, S8)**. Notably, PCA1.5-PEG5 NPs displayed a well-defined core-shell morphology with uniformly distributed particles **(Figure 3c, S9),** indicating more controlled NPs assembly. Dynamic light scattering (DLS) analysis of PCA1.5-PEG5 revealed a uniform hydrodynamic diameter (D_h) of 109 nm and a polydispersity index (PDI) of 0.19 **(Figure 3d)**. To further optimize the NPs, the effect of DSPE-PEG stock was evaluated by preparing NPs 5, 10, and 20 mg/mL DSPE-PEG while keeping the polymer constant (PCA1.5h). The formulation containing 5 mg/mL DSPE-PEG (PCA1.5-PEG 5 NPs) exhibited the most uniform size distribution, lowest PDI and higher ζ-potential compared to PCA1.5-PEG10 and PCA1.5-PEG20 (**Figure 3e, S6**). The reduced ζ-potential at higher DSPE-PEG concentrations could be attributed to increased surface shielding by the PEG corona.[28] Finally, the colloidal stability of the optimized PCA1.5-PEG5 NPs was further assessed over 7 days under three different storage conditions (37 °C, 4 °C, and plasma). The NPs maintained consistent size distributions with minimal variations, indicating good colloidal stability under all tested conditions (**Figure 3f**).

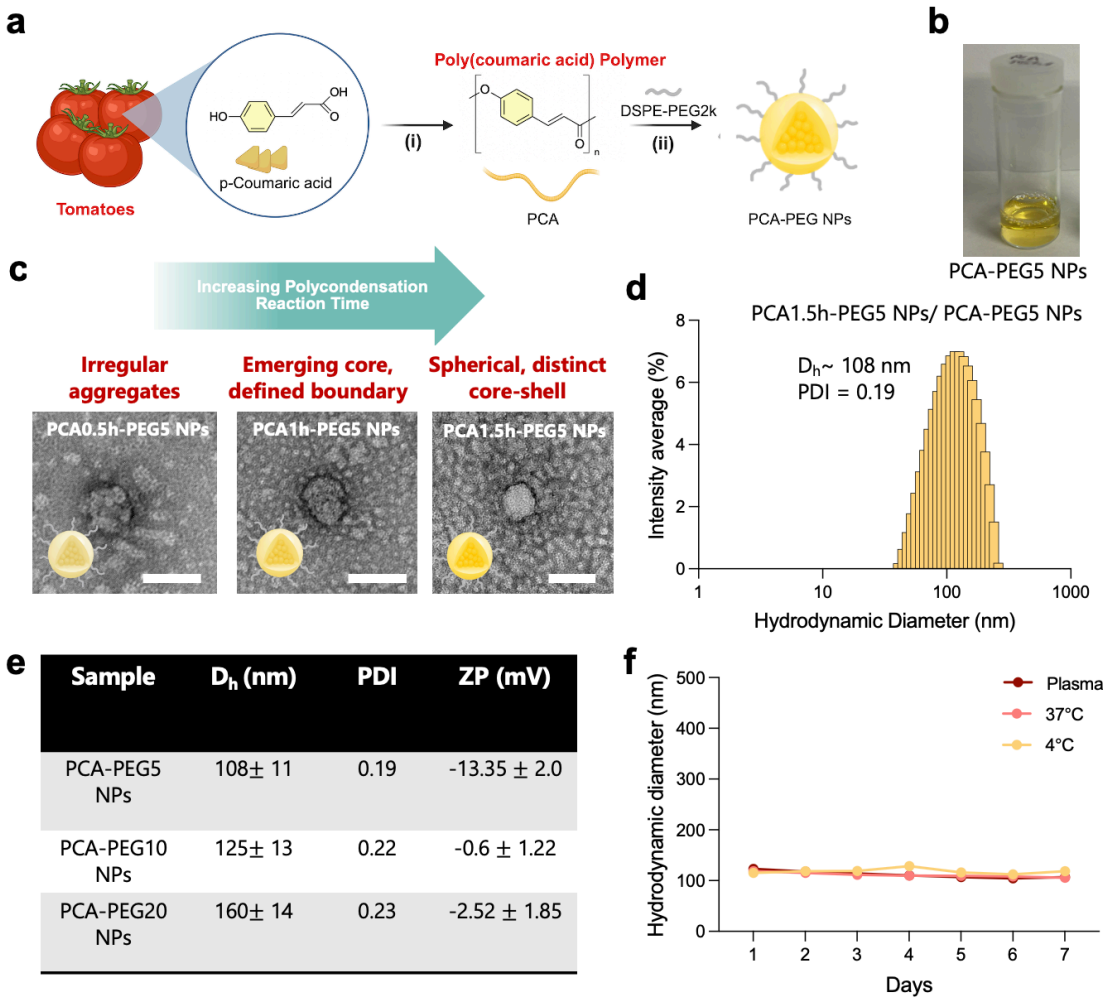

Sample	D_h (nm)	PDI	ZP (mV)
PCA-PEG5 NPs	108± 11	0.19	-13.35 ± 2.0
PCA-PEG10 NPs	125± 13	0.22	-0.6 ± 1.22
PCA-PEG20 NPs	160± 14	0.23	-2.52 ± 1.85

Figure 3. Synthesis, optimization, and physicochemical characterization of PCA-PEG NPs. (a) Schematic overview of PCA-PEG-ICG NPs synthesis using P-Coumaric acid polymer (b) Representative photograph of the formulated PCA1.5-PEG5 NPs (c) TEM images of PCA0.5h-PEG5NPs, PCA1h-PEG5 NPs and PCA1.5h-PEG NPs. Scale bar = 100 nm. (d) Hydrodynamic diameter intensity graph of PCA1.5h-PEG5 NPs (e) Hydrodynamic diameter, PDI, and ζ-potential values of PCA-PEG5NPs, PCA-PEG10 NPs and PCA-PEG20 NPs. (f) Colloidal stability of PCA1.5h-PEG5 NPs over 7 days while incubated at 37°C, 4°C and 37°C with plasma.

Synthesis and Comprehensive Physicochemical and Optical Characterization of PCA-PEG5-ICG NPs. Building on the optimized PCA1.5-PEG5 formulation, NPs were engineered to encapsulate indocyanine green (ICG), an FDA approved near-infrared (NIR) fluorescent dye, to impart imaging functionality.[20, 29] ICG was co-dissolved with PCA in DMSO and subsequently added dropwise into PBS under continuous probe sonication to form PCA-PEG5-ICG NPs **(Figure 4a)**. Following purification *via* washing and filtration **(figure 4b)**, the physiochemical and optical properties of the NPs were characterized. The DLS measurements revealed a hydrodynamic measurement of 127.2 nm and a low PDI, while ζ-potential values were around -11.3 mV indicated good colloidal stability **(Figure 4c, d)**. Importantly, these properties were comparable to those of uncoated NPs, suggesting that ICG did not significantly alter the NPs characteristics. UV-Vis spectroscopy of PCA1.5-PEG5-ICG NPs showed a characteristic peak ~ 800 nm corresponding to encapsulated ICG **(Figure 4e)**, while fluorescence measurements (λ_{ex} = 785nm) demonstrated strong NIR-I emission with an emission maxima at 846nm **(Figure 4f)**. Fluorescence imaging *via* IVIS imaging further confirmed robust signal intensity compared to controls, with a concentration-dependent increase observed across serial dilutions **(Figure 4g, h)**. Given the known limitations of free ICG, including poor photostability and aggregation in aqueous environments[30], we next evaluated fluorescence stability over time. PCA-PEG5-ICG NPs maintained stable fluorescence signal intensity over a period of 7 days, whereas free ICG exhibited substantial signal decay, highlighting the protective role of the PCA-PEG matrix **(Figure 4i)**.

Colloidal stability was further assessed by comparing PCA 1.5-PEG-ICG NPs with lower polymer formulations (PCA1-PEG5-ICG NPs and PCA0.5-PEG5-ICG-NPs) under physiological (37°C), 37°C with plasma, and refrigerated (4°C) for 7 days. PCA1.5-PEG-ICG showed minimal

fluctuations in hydrodynamic size across all conditions, indicating high colloidal stability across all conditions, indicating improved colloidal stability relative to other formulations **(Figure 4j)**. Such behavior could be attributed to the increased polymer length, leading to a higher encapsulation efficiency of PCA1.5-PEG5-ICG NPs in comparison to its counterparts **(Figure S10),** reducing ICG aggregation and providing protection against photodegradation.

To better approximate the optical complexity of tumor environments, fluorescence performance was evaluated in the presence of intralipid, a scattering medium that mimics soft tissue. Notably, increasing intralipid concentration did not significantly attenuate fluorescence intensity, indicating strong signal retention under highly scattering conditions **(Figure 4k, S11)**. Furthermore, evaluation within TMPs composed of intralipid and hemoglobin **(Figures S13, S14)** demonstrated detectable fluorescence even at low concentrations, supporting the suitability of PCA-PEG5-ICG nanoparticles for imaging in complex tissue-like environments.

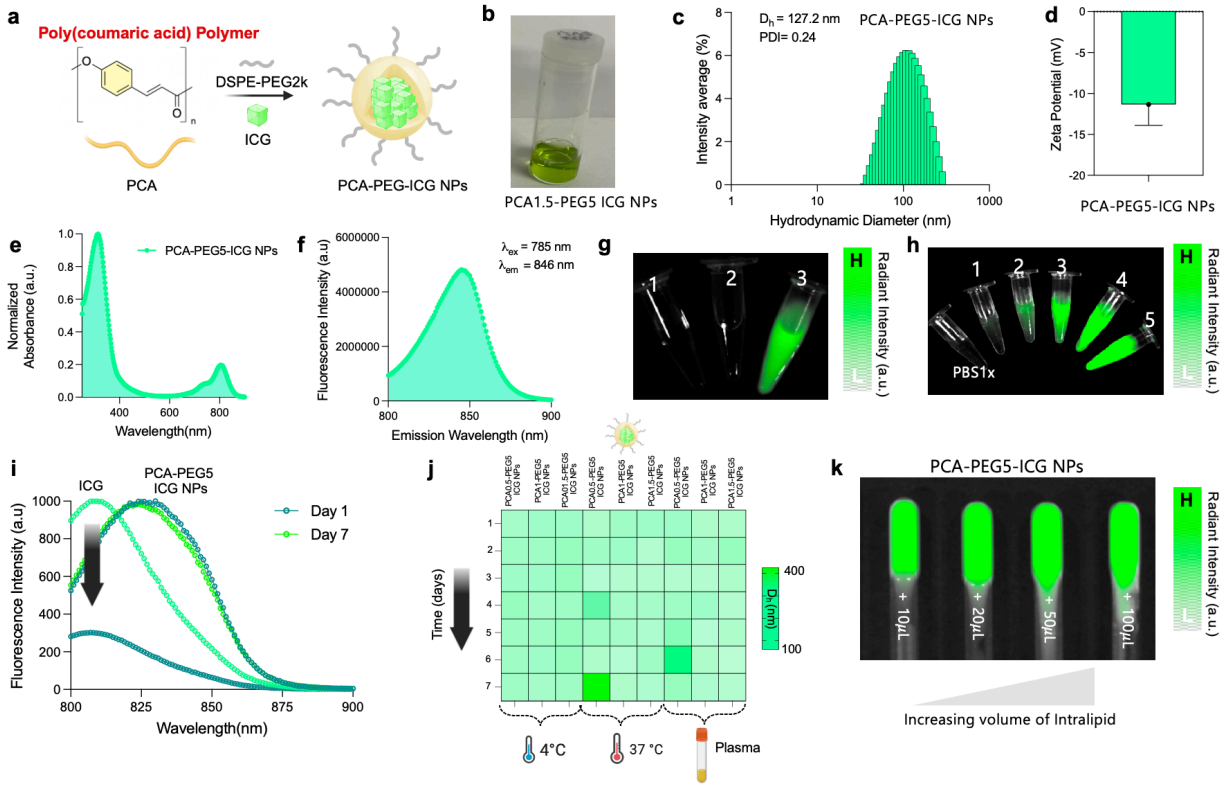

Figure 4. Preparation, physiochemical and optical characterization of PCA-PEG5-ICG NPs. (a) Schematic overview of PCA-PEG-ICG NPs synthesis (b) Representative white light photograph of the formulated PCA1.5-PEG-ICG NPs (c) and (d) Hydrodynamic diameter intensity graph and Zeta potential (mV) of PCA-PEG-ICG NPs. (e) UV-VIS absorbance spectra of PCA-PEG-ICG NPs and (f) Fluorescence intensity of PCA-PEG-ICG NPs. (g) NIR-I fluorescence imaging of (1) PBS-1X (2) PCA1.5-PEG NPs (3) PCA1.5-PEG-ICG NPs. (h) NIR-I fluorescence imaging of PBS1X and PCA-PEG-ICG NPs, where 5: 7.3 μM , 4: 3.5 μM, 3: 1.9 μM, 2: 0.69 μM and 1: 0.12 μm of ICG. (i) Fluorescence stability of PCA-PEG-ICG NPs and free ICG evaluated on day 1 and day 7. (j) Colloidal stability of PCA0.5-PEG-ICG NPs, PCA1-PEG-ICG NPs and PCA1.5-PEG-ICG NPs over 7 days while incubated at 37°C, 4°C and 37°C with plasma. (k) NIR-I fluorescence imaging of PCA1.5h-PEG5-ICG NP in an NMR tube with increasing volume of intralipid.

Assessment of *In Vitro* Cytotoxicity, Cellular Internalization and Biological Activity of PCA-PEG5 and PCA-PEG5-ICG NPs. Coumaric acid possesses intrinsic cytotoxic and oxidative stress-modulating properties.[17, 25, 31] We hypothesized that the synthesis of PCA would provide a high-density, prodrug scaffold capable of being formulated in stable NPs via nanoprecipitation. We further anticipated that increasing the PCA chain length would enhance lysosomal delivery. Once internalized, the acidic enzymes will cause the degradation of the polymer backbone into its constitutive CA monomers, triggering cytosolic release and sustained anticancer activity.[14, 16] To evaluate this, we compared the cytotoxic profiles of PCA0.5-PEG5 NPs, PCA1-PEG5 and PCA1.5-PEG5 NPs. As shown in **Figure 5a, b,** PCA1.5-PEG5 NPs induced significantly higher cell death compared to the lower-order formulations (PCA0.5-PEG5, PCA1-PEG5 NPs), consistent with our hypothesis. As expected, PEG5 NPs, lacking PCA did not show any change in cell death across increasing concentrations (**Figure S12**)

Since the therapeutic efficacy is fundamentally governed by internalization efficiency, we employed IVIS imaging to quantify NPs uptake into OVCAR8 cells **(Figure 5c)**. Given their superior cytotoxicity, PCA1.5-PEG5-ICG NPs were prioritized for cellular uptake profiling. Fluorescence quantification (**Figure 5d**) revealed time-dependent increase in internalization, reaching peak uptake at 24 h**.** Recognizing that there is a strong correlation between cellular uptake and the physicochemical properties of NPS including shape, surface charge and stability, [28, 32, 33] we benchmarked PCA0.5-PEG5-ICG and PCA1-PEG5-ICG NPs at the 24 h. As shown in **Figure 5e**, PCA1.5-PEG5-ICG NPs exhibited the highest cellular internalization amongst all formulations, further elucidating the correlation between macromolecular architecture, cellular internalization, and resulting cytotoxic efficacy.

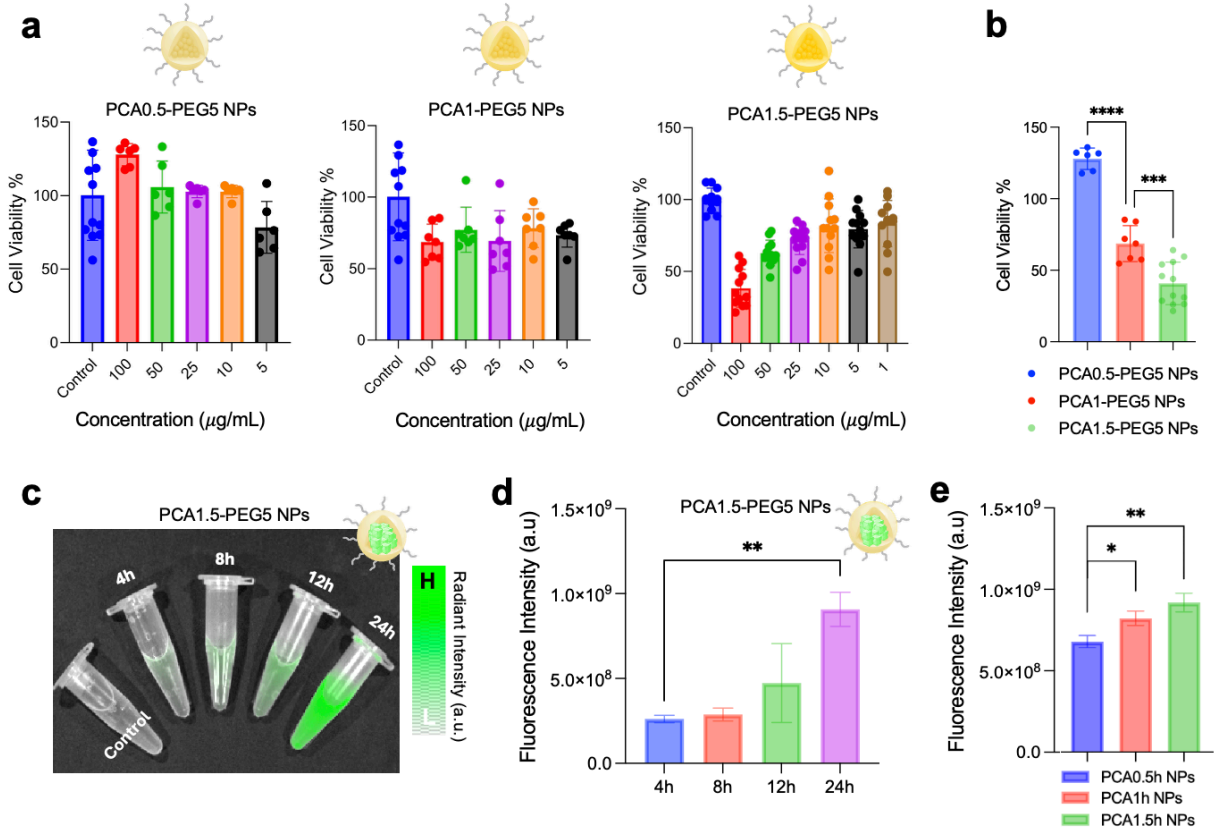

Figure 5. *In-vitro* evaluation of cytotoxicity, cellular uptake, and biological activity of PCA-PEG NPs. (a) Cell viability of OVCAR8 following treatment with PCA0.5-PEG NPs, PCA1-PEG NPs and PCA1.5-PEG NPs. (b) Comparative analysis of cell viability in OVCAR8 following treatment with 100 μg/ml PCA0.5-PEG NPs, PCA1-PEG NPs and PCA1.5-PEG NPs. (c) NIR-I fluorescence imaging of OVCAR8 following treatment with PCA1.5-PEG-ICG NPs at 4h, 8h, 12 and 24h. (d) Quantification of fluorescence intensity of OVCAR8 following treatment with PCA1.5-PEG-ICG NPs at 4h, 8h, 12 and 24h showing a time dependent internalization. (e) Quantification of fluorescence intensity of OVCAR8 following treatment with PCA0.5-PEG-ICG NPs, PCA1-PEG-ICG NPs and PCA1.5-PEG-ICG NPs at 24h.

Photobleaching and Photostability Evaluation of PCA-PEG-ICG Nanoparticles. Fluorescence based imaging is frequently limited by photobleaching, particularly for clinically used fluorophores such as ICG, which undergo rapid signal degradation under continuous illumination. This primarily occurs due to the photoinduced interactions with molecular oxygen and reactive species that result in irreversible structural degradation.[34-36]

Photostability of our PCA-PEG-ICG NPs was evaluating tumor-mimicking phantoms (TMPs), previously developed by us [20-22, 37], which more closely recapitulates the optical and absorption characteristics of tumors compared to conventional *in vitro* measurements. Upon continuous white light excitation (1000 lumens) (**Figure S15**), PCA-PEG-ICG NPs TMPs retained strong fluorescence over a 4h period, whereas free ICG at similar concentrations exhibited rapid signal decay under identical conditions (**Figure 6b, c**). Control TMPs without any contrast agents showed negligible signal. Quantitative analysis of radiant intensity confirmed significantly improved fluorescence retention for PCA-PEG-ICG NPs in TMPs relative to free ICG in TMPs, highlighting the stability effect of the NPs.

The enhanced photostability can be attributed to multiple synergistic effects of the PCA matrix. First, the polymeric network acts as a physical barrier that limits oxygen diffusion and reduces direct interaction of excited ICG with external quenchers.[38-41] Second, the phenolic functionality of PCA provides intrinsic antioxidant activity, enabling scavenging of reactive oxygen species generated during photoexcitation and thereby suppressing oxidative degradation pathways.[15, 17, 23] Additionally, encapsulation within the hydrophobic polymer matrix reduces dye aggregation and restricts conformational flexibility, helping to maintain ICG in a more stable and dispersed state.[38]

Tissue penetration profiling under clinically relevant settings was further performed to evaluate the optical performance of PCA-PEG-ICG NPs. Layered *ex vivo* porcine tissues (muscle, fat, and skin) were used to simulate relevant optical barriers and varying penetration depth (0, 2, 4 mm) **(Figure S16)**. Compared to ICG TMPs at equivalent concentrations, PCA-PEG-ICG NPs TMPs consistently exhibited higher fluorescence intensity across all tissue types and increasing depths **(Figure S17-S19)**. The enhanced signal propagation through tissue is attributed to the improved stability and preserved fluorescence of ICG within the PCA matrix, which mitigates signal loss under attenuating conditions. These results further highlight the ability of the PCA-based nanoparticle system to maintain fluorescence output in optically challenging environments, supporting its potential for improved intraoperative imaging, particularly in deeper or highly scattering tissues.

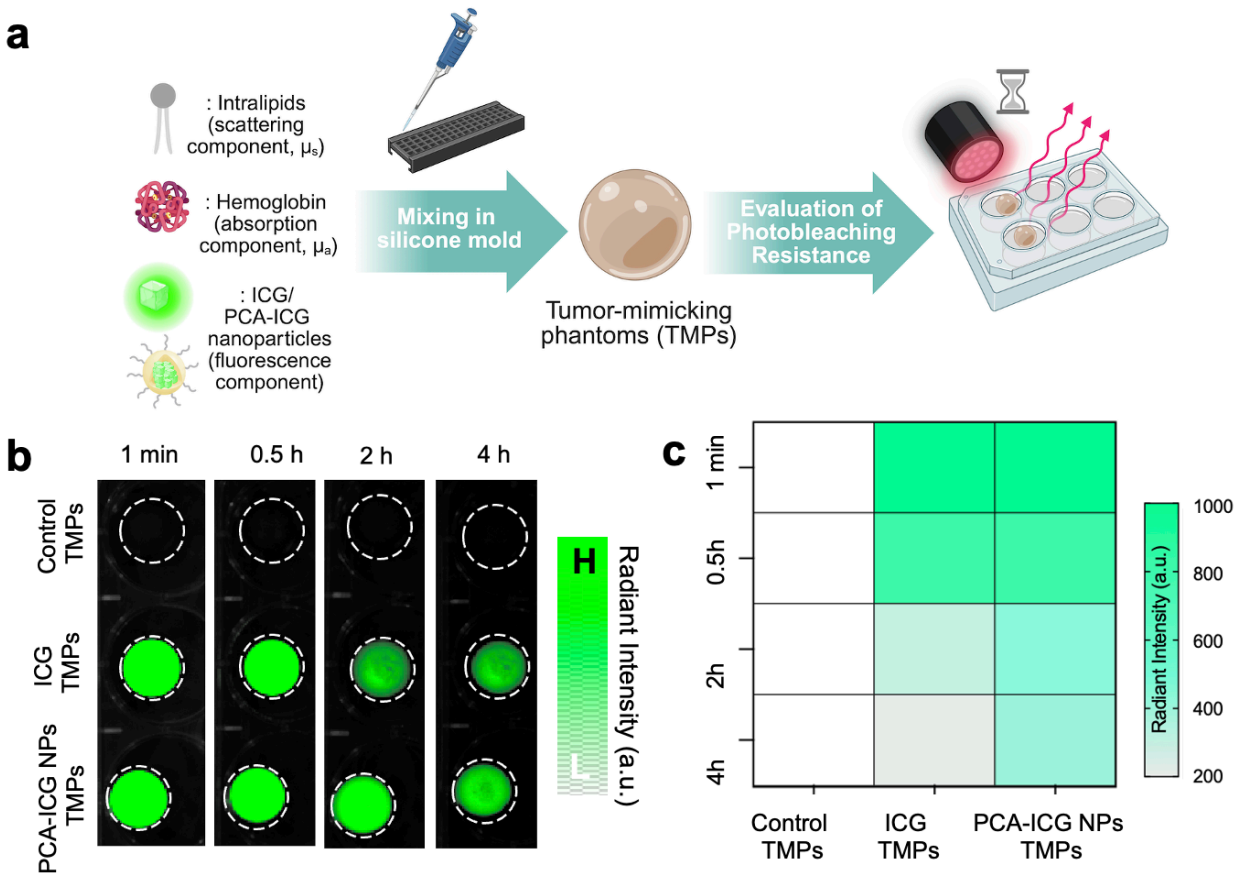

Figure 6. Photobleaching assessment of PCA-PEG-ICG NP TMPs compared to clinical standard, ICG. (a) Schematic diagram of preparation of PCA-PEG-ICG NPs and ICG TMPs and their photostability evaluation. (b) NIR-I fluorescence image of Control TMP, PCA-ICG NP TMP and ICG TMP after being subject to 1000 lumen white light source for different time durations (1min, 0.5h, 2h, 4h). (c) Corresponding radiant fluorescence intensity measurements for (b). Experiments were done in triplicates.

Performing Surgical Simulation on 3D-printed Intraperitoneal Tumor Phantoms. Building on our previously reported 3D tumor-mimicking phantoms (TMPs) platform,[20-22, 37] which enables precise control over tissue optical properties and tumor composition through a customizable bioprinted bioink, we sought to extend this system to more clinically relevant cancer scenarios. Intraperitoneal (IP) tumors represent a particularly challenging and clinically relevant model for evaluating image-guided surgical approaches due to their diffuse anatomical distribution, the frequent requirement for extensive cytoreductive surgery (CRS) to remove multiple scattered nodules, and a heterogeneous microenvironment that limits the effectiveness of conventional therapies.[42-45]

While our prior TMPs constructs effectively recapitulated the optical and structural features of individual tumors, they did not capture the multifocal and spatially heterogeneous nature of IP metastases,[46-48] where numerous tumor nodules are distributed throughout the abdominal cavity. To address this limitation, we developed a 3D bioprinted IP tumor model incorporating multiple TMPs within a tissue mimicking-environment to replicate the nodule dissemination observed within an IP tumor-bearing mice (**Figure 7a**). To further approximate physiological imaging conditions, we fabricated subcutaneous skin-mimicking layers with tunable melanin concentrations **(Figure S20)** to replicate the optical attenuation and scattering imposed by overlaying tissues, which subsequently influences fluorescence signal propagation during *in vivo* imaging of IP tumors.

TMPs were generated using our established bioink formulation containing optical scatterers (Intralipid), absorbers (hemoglobin), and a gelatin-based biomimetic matrix, along with PCA-

PEG-ICG NPs as the functional imaging agent. This system enables precise control over tumor geometry, composition, and spatial distribution within a precisely controlled matrix. These printed constructs were integrated into a simulated intraperitoneal environment **(Figure S21)**, allowing evaluation of NPs performance under conditions that closely recapitulate *in vivo* imaging scenarios.

Fluorescence-guided surgical resection was then performed to simulate image-guided surgery, enabling real-time visualization of tumor margin and assessment of nanoprobe distribution and contrast during resection **(Figure 7b, d)**. This platform allowed systematic evaluation of NPs performance under dynamic settings, including tissue-like scattering, repeated light exposure, and partial resections that mimic intraoperative procedures. Importantly, residual tumor-to-background signal post-resection was quantified to assess the ability of NPs to identify incompletely removed tumor foci **(Figure 7c, e)**. Overall, this 3D bioprinted platform provides a reliable and reproducible method for studying NPs-assisted tumor delineation, intraoperative decision-making and resection accuracy in a clinically relevant context, effectively bridging the gap between simplified *in vitro* assessments and complex *in vivo* studies.

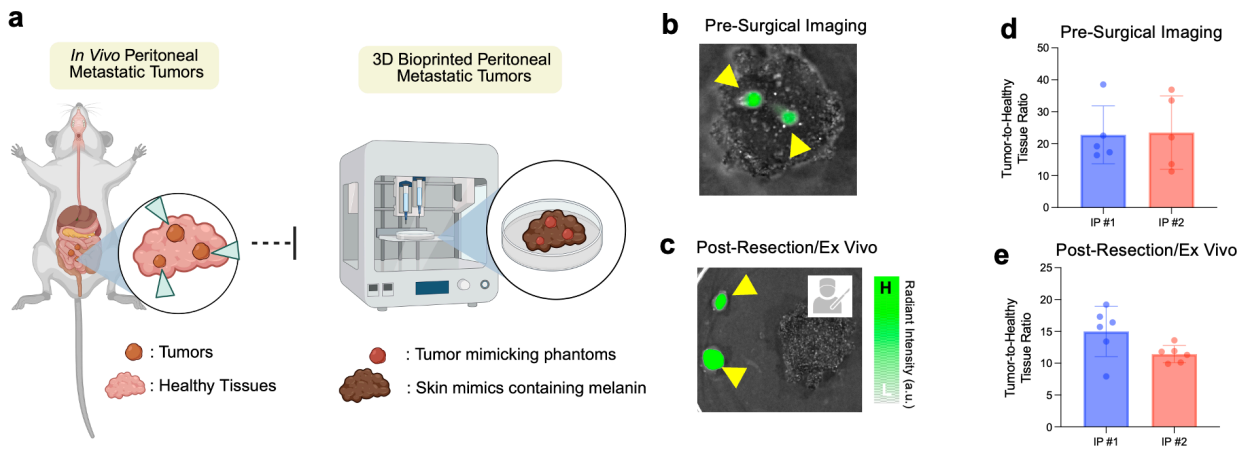

Figure 7. 3D Printing of intraperitoneal tumors to simulate *ex vivo* image-guided surgery. (a) Schematic showing *In Vivo* Peritoneal Metastatic Tumors and 3D Printing of Intraperitoneal Tumors on Skin Mimic using 3D Bioprinter. NIR-I Fluorescence images of (b) pre-surgical and (c) post-surgical simulation showing resection of intraperitoneal tumors. Corresponding tumor-to-healthy tissue ratio quantification of (d) pre-surgical and (e) post-surgical simulation.

Hemocompatibility Assessments of PCA-PEG5 NPs. Assessing how nanoprobes interact with red blood cells is a critical early step in determining their biocompatibility. In this study, we measured hemolysis, defined as the rupture of erythrocytes, after incubating porcine red blood cells with PCA-PEG5 nanoparticles at varying concentrations (1, 5, 10, 50, and 100 µg/mL). Standard controls were included for comparison: phosphate-buffered saline (PBS1x) served as the negative control, while deionized water acted as the positive control. All samples treated with PCA-PEG5 nanoparticles showed intact red blood cell pellets at the bottom of the tubes, indicating that cell integrity was maintained. In contrast, samples exposed to deionized water exhibited complete hemolysis, as shown by a uniformly red supernatant and the absence of a pellet. The PBS1x control produced a compact pellet with a clear supernatant, consistent with minimal

hemolysis. Across all tested concentrations, PCA-PEG5 nanoparticles induced hemolysis levels below the 10% threshold considered acceptable for blood compatibility, with the lowest value observed at 10 µg/mL (3.12 ± 1.08%). These findings demonstrate that the nanoprobes are hemocompatible within the tested concentration range and are unlikely to cause red blood cell damage under physiological conditions.

Overall, these preliminary results suggest minimal toxicity in healthy porcine blood at the evaluated doses, supporting their potential use for *in vivo* applications. Nonetheless, more comprehensive studies are needed to assess both short- and long-term toxicity across a wider range of doses in living systems, which falls beyond the scope of this work.

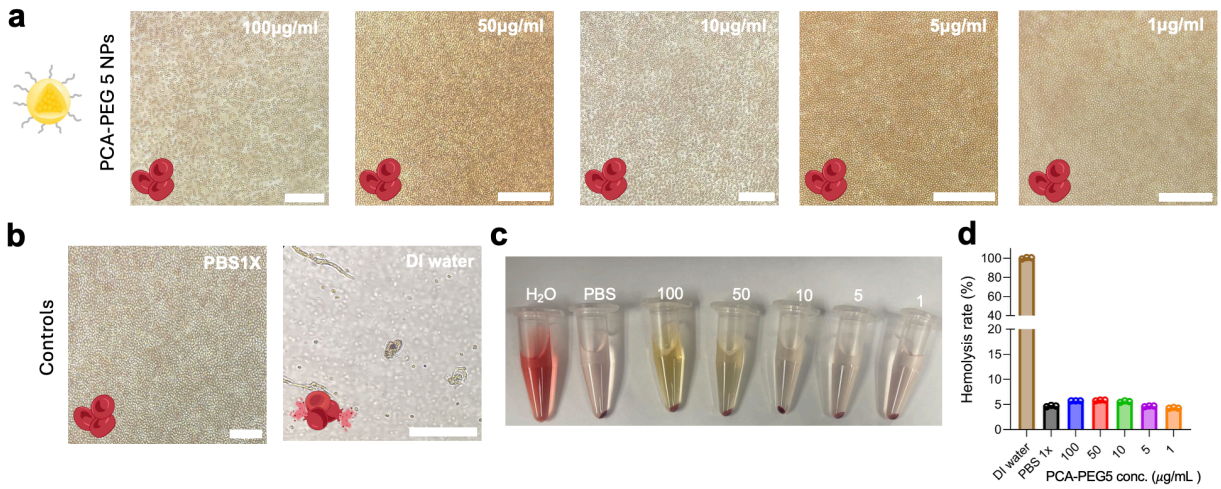

Figure 8. Hemocompatibility studies of PCA-PEG5 NPs with porcine blood. Inverted microscopic images at 200× magnification of (a) PCA-PEG5 NPs (100, 50, 10, 5, and 1 µg/mL), (b) PBS1x (negative control), and DI water (positive control) after 1h of incubation at 37 °C with porcine blood. (c) White light image of RBC pellets from each incubated sample: (1) 100 µg/mL,

(2) 50 μg/mL, (3) 10 μg/mL, (4) 5 μg/mL, (5) 1 μg/mL, (6) PBS1x, and (7) DI water. (d) Relative hemolysis percentages of all PCA-PEG5 treatment and control groups.

CONCLUSIONS.

In summary, we report the development of self-theranostic hybrid nanoparticles in which the macromolecular architecture of the PCA core serves as a key determinant of both optical and colloidal performances, cellular endocytosis behavior, and therapeutic efficacy. By tuning the polymer structure through variation in polycondensation reaction time, we demonstrate that extended reaction durations promote the formation of more robust polymer backbones, enabling improved core-shell assembly. This optimized architecture enhances the hydrophobic sequestration and photostability of encapsulated ICG, a representative NIR-I fluorophore, effectively mitigating the rapid quenching and degradation associated with free dye systems.

Beyond its structural role, the PCA matrix functions as a redox-active, self-therapeutic scaffold. The nanoparticles exhibit preferential internalization in ovarian cancer cells, where the phenolic backbone modulates intracellular oxidative stress, ultimately inducing apoptosis. The dual imaging-therapeutic functionality was further validated using 3D bioprinted intraperitoneal tumor models, where the nanoprobes enabled high-contrast and photostable fluorescence for surgical guidance under optically complex conditions.

Overall, this work establishes polymer architecture, governed by controllable synthetic parameters, as a critical design variable in the development of integrated nanomedicines. This structure-guided approach provides a versatile framework for engineering multifunctional

platforms that synchronize diagnostic imaging with intrinsic biological activity, advancing the design of next-generation systems for precision cancer intervention.

AUTHOR INFORMATION

Corresponding Author

*Indrajit.srivastava@ttu.edu

Author Contributions

+ M. M., A. H., and K. K. contributed equally. I. S. conceived the idea and design the experiments. M. M., A. H., and K. K. were involved in data collection and curation, formal analysis, investigation, methodology, validation, and visualization of all the experiments under the supervision of I.S. 3D bioprinting of TMPs were conducted by I. D. L. under the supervision of I.S. M.H.R. performed transmission electron microscopy images.

ACKNOWLEDGMENT

I.S. acknowledges the Edward E. Whitacre Jr. College of Engineering and Texas Tech University for research support.

REFERENCES

(1) Fan, X.; Liu, X.; Xia, Q.; Chen, G.; Cheng, J.; Shi, Z.; Fang, Y.; Khadaroo, P. A.; Qian, J.; Lin, H. Advanced Image-Guidance and Surgical-Navigation Techniques for Real-Time Visualized Surgery. *Advanced Science* **2025**, *12* (41). DOI: 10.1002/advs.202509294.

(2) Wang, K.; Du, Y.; Zhang, Z.; He, K.; Cheng, Z.; Yin, L.; Dong, D.; Li, C.; Li, W.; Hu, Z.; et al. Fluorescence image-guided tumour surgery. *Nature Reviews Bioengineering* **2023**, *1* (3), 161–179. DOI: 10.1038/s44222-022-00017-1.

(3) Leiloglou, M.; Kedrzycki, M. S.; Chalau, V.; Chiarini, N.; Thiruchelvam, P. T. R.; Hadjiminas, D. J.; Hogben, K. R.; Rashid, F.; Ramakrishnan, R.; Darzi, A. W.; et al. Indocyanine green fluorescence image processing techniques for breast cancer macroscopic demarcation. *Scientific Reports* **2022**, *12* (1). DOI: 10.1038/s41598-022-12504-x.

(4) Gamage, R. S.; Smith, B. D. Fluorescence Imaging Using Deep-Red Indocyanine Blue, a Complementary Partner for Near-Infrared Indocyanine Green. *Chemical & Biomedical Imaging* **2024**, *2* (5), 384–397. DOI: 10.1021/cbmi.4c00008.

(5) Jing, L.; Shi, J.; Fan, D.; Li, Y.; Liu, R.; Dai, Z.; Wang, F.; Tian, J. ¹⁷⁷Lu-Labeled Cerasomes Encapsulating Indocyanine Green for Cancer Theranostics. *ACS Applied Materials & Interfaces* **2015**, *7* (39), 22095–22105. DOI: 10.1021/acsami.5b07856.

(6) Feng, S.; Chen, J.; Wo, Y.; Li, Y.; Chen, S.; Zhang, Y.; Zhang, W. Real-time and long-time in vivo imaging in the shortwave infrared window of perforator vessels for more precise

evaluation of flap perfusion. *Biomaterials* **2016**, *103*, 256–264. DOI: 10.1016/j.biomaterials.2016.06.043.

(7) Liu, D.; Wang, Y.; Xue, F.; Fu, J.; Zhao, X.; Song, S.; Gu, J. Comparative analysis of indocyanine green dosages for optimal fluorescence imaging in laparoscopic cholecystectomy. *Scientific Reports* **2025**, *15* (1). DOI: 10.1038/s41598-025-97912-5.

(8) Hill, T. K.; Abdulahad, A.; Kelkar, S. S.; Marini, F. C.; Long, T. E.; Provenzale, J. M.; Mohs, A. M. Indocyanine Green-Loaded Nanoparticles for Image-Guided Tumor Surgery. *Bioconjugate Chemistry* **2015**, *26* (2), 294–303. DOI: 10.1021/bc5005679.

(9) An, F.; Yang, Z.; Zheng, M.; Mei, T.; Deng, G.; Guo, P.; Li, Y.; Sheng, R. Rationally assembled albumin/indocyanine green nanocomplex for enhanced tumor imaging to guide photothermal therapy. *Journal of Nanobiotechnology* **2020**, *18* (1). DOI: 10.1186/s12951-020-00603-8.

(10) Lv, Q.; Song, W.; Chu, J.; Li, G.; Han, Y.; Marfavi, Z.; Zhang, G.; Wu, Y.; Lin, Y.; Sun, K.; et al. An Indocyanine Green-Based Nanocluster for Imaging Orthodox Endometriosis Lesions with Negative Contrast. *ACS Applied Materials & Interfaces* **2024**, *16* (20), 25909–25922. DOI: 10.1021/acsami.4c04131.

(11) Mirkin, C. A.; Mrksich, M.; Artzi, N. The emerging era of structural nanomedicine. *Nature Reviews Bioengineering* **2025**, *3* (7), 526–528. DOI: 10.1038/s44222-025-00306-5.

(12) Mirkin, C. A.; Langer, R.; Mrksich, M.; Margolin, A. A.; Petrosko, S. H.; Artzi, N. Blueprints for Better Drugs: The Structural Revolution in Nanomedicine. *ACS Nano* **2025**, *19* (20), 18889–18901. DOI: 10.1021/acsnano.5c06380.

(13) Wu, S.; Yuan, M.; Han, S.; Wang, L.; You, X.; Wu, J. Development of poly(ρ-coumaric acid) based nanodrug delivery system incorporating hyaluronic acid for enhanced wound

healing. *RSC Applied Polymers* **2025**, *3* (5), 1278–1288, 10.1039/D5LP00107B. DOI: 10.1039/D5LP00107B.

(14) Ou, K.; Xu, X.; Guan, S.; Zhang, R.; Zhang, X.; Kang, Y.; Wu, J. Nanodrug Carrier Based on Poly(Ursolic Acid) with Self-Anticancer Activity against Colorectal Cancer. *Advanced Functional Materials* **2020**, *30* (9), 1907857. DOI: https://doi.org/10.1002/adfm.201907857.

(15) Nie, Y.; Wang, L.; Liu, S.; Dai, C.; Cui, T.; Lei, Y.; You, X.; Wang, X.; Wu, J.; Zheng, Z. Natural ursolic acid based self-therapeutic polymer as nanocarrier to deliver natural resveratrol for natural therapy of acute kidney injury. *Journal of Nanobiotechnology* **2023**, *21* (1). DOI: 10.1186/s12951-023-02254-x.

(16) Li, Y.; Cai, B.; Zhang, Z.; Qu, G.; Chen, L.; Chen, G.; Liang, T.; Yang, C.; Fan, L.; Zhang, Z. Salicylic acid-based nanomedicine with self-immunomodulatory activity facilitates microRNA therapy for metabolic skeletal disorders. (1878-7568 (Electronic)). From 2021 Aug.

(17) Wang, L.; You, X.; Dai, C.; Fang, Y.; Wu, J. Development of poly(p-coumaric acid) as a self-anticancer nanocarrier for efficient and biosafe cancer therapy. *Biomaterials Science* **2022**, *10* (9), 2263–2274, 10.1039/D2BM00027J. DOI: 10.1039/D2BM00027J.

(18) You, X.; Wang, L.; Wang, L.; Wu, J. Rebirth of Aspirin Synthesis By-Product: Prickly Poly(salicylic acid) Nanoparticles as Self-Anticancer Drug Carrier. *Advanced Functional Materials* **2021**, *31* (33), 2100805. DOI: https://doi.org/10.1002/adfm.202100805.

(19) Choodet, C.; Toomjeen, P.; Chuaephon, A.; Phanchai, W.; Srikulwong, U.; Wiwasuku, T.; Puangmali, T. Polymeric Nanoparticles Engineered for Optimal Drug Delivery Using Atomistic Computational Simulation. *ACS Applied Nano Materials* **2024**, *7* (16), 19698–19708. DOI: 10.1021/acsanm.4c03894.

(20) Harun, A.; Bendele, N.; Khalil, M. I.; Vasquez, I.; Djuanda, J.; Posey, R.; Rashid, M. H.; Christopher, G. F.; Bickel, U.; Gruev, V.; et al. 3D Tumor-Mimicking Phantom Models for Assessing NIR I/II Nanoparticles in Fluorescence-Guided Surgical Interventions. *ACS Nano* **2025**, *19* (21), 19757–19776. DOI: 10.1021/acsnano.5c01919.

(21) Vasquez, I.; Harun, A.; Posey, R.; Reddy, R.; Gill, N.; Bickel, U.; Tropp, J.; Srivastava, I. Ultrabright NIR-II Nanoprobes for Ex Vivo Bioimaging: Protein Nanoengineering Meets Molecular Engineering. *ACS Nanoscience Au* **2025**, *5* (6), 527–542. DOI: 10.1021/acsnanoscienceau.5c00100.

(22) Bendele, N.; Kitamura, K.; Vasquez, I.; Harun, A.; Carroll, M.; Srivastava, I. Near-Infrared Afterglow Luminescence Amplification via Albumin Complexation of Semiconducting Polymer Nanoparticles for Surgical Navigation in Ex Vivo Porcine Models. *Advanced Functional Materials* **2024**, *34* (38), 2407753. DOI: https://doi.org/10.1002/adfm.202407753.

(23) Meng, Y.; Han, S.; Yin, J.; Wu, J. Therapeutic Copolymer from Salicylic Acid and l-Phenylalanine as a Nanosized Drug Carrier for Orthotopic Breast Cancer with Lung Metastasis. *ACS Applied Materials & Interfaces* **2023**, *15* (35), 41743–41754. DOI: 10.1021/acsami.3c08608.

(24) Hayashi, S.; Yamamoto, S.-i.; Koizumi, T. Effects of molecular weight on the optical and electrochemical properties of EDOT-based π-conjugated polymers. *Scientific Reports* **2017**, *7* (1), 1078. DOI: 10.1038/s41598-017-01132-5.

(25) Yoon, J.-H.; Youn, K.; Ho, C.-T.; Karwe, M. V.; Jeong, W.-S.; Jun, M. p-Coumaric Acid and Ursolic Acid from Corni fructus Attenuated β-Amyloid25–35-Induced Toxicity through Regulation of the NF-κB Signaling Pathway in PC12 Cells. *Journal of Agricultural and Food Chemistry* **2014**, *62* (21), 4911–4916. DOI: 10.1021/jf501314g.

(26) Vuković, L.; Khatib, F. A.; Drake, S. P.; Madriaga, A.; Brandenburg, K. S.; Král, P.; Onyuksel, H. Structure and Dynamics of Highly PEG-ylated Sterically Stabilized Micelles in Aqueous Media. *Journal of the American Chemical Society* **2011**, *133* (34), 13481–13488. DOI: 10.1021/ja204043b.

(27) Liu, Y.; Shipton, M. K.; Ryan, J.; Kaufman, E. D.; Franzen, S.; Feldheim, D. L. Synthesis, Stability, and Cellular Internalization of Gold Nanoparticles Containing Mixed Peptide−Poly(ethylene glycol) Monolayers. *Analytical Chemistry* **2007**, *79* (6), 2221–2229. DOI: 10.1021/ac061578f.

(28) Devalapally, H.; Zhou, F.; McDade, J.; Goloverda, G.; Owen, A.; Hidalgo, I. J.; Silchenko, S. Optimization of PEGylated nanoemulsions for improved pharmacokinetics of BCS class II compounds. *Drug Delivery* **2015**, *22* (4), 467–474. DOI: 10.3109/10717544.2013.869275.

(29) Sun, Y.-T.; Chen, M.-H.; Lai, H.-W.; Hsu, T.-H.; Chin, Y.-H.; Tseng, S.-M.; Lai, S.-C.; Lin, C.-A. J. Unravelling the Tunable Near-Infrared-II Fluorescence from FDA-Approved Indocyanine Green via Supramolecular Complexation with Albumin. *ACS Applied Bio Materials* **2026**. DOI: 10.1021/acsabm.5c02548.

(30) Xia, W.-L.; Ran, X.-Y.; Xie, K.-P.; Zhao, Y.; Chen, J.; Zhou, Q.; Yu, X.-Q.; Li, K. Optimized indocyanine green nanopreparations for biomedical applications. *Coordination Chemistry Reviews* **2025**, *528*, 216422. DOI: https://doi.org/10.1016/j.ccr.2024.216422.

(31) Nasr Bouzaiene, N.; Kilani Jaziri, S.; Kovacic, H.; Chekir-Ghedira, L.; Ghedira, K.; Luis, J. The effects of caffeic, coumaric and ferulic acids on proliferation, superoxide production, adhesion and migration of human tumor cells in vitro. *European Journal of Pharmacology* **2015**, *766*, 99–105. DOI: https://doi.org/10.1016/j.ejphar.2015.09.044.

(32) Niikura, K.; Matsunaga, T.; Suzuki, T.; Kobayashi, S.; Yamaguchi, H.; Orba, Y.; Kawaguchi, A.; Hasegawa, H.; Kajino, K.; Ninomiya, T.; et al. Gold Nanoparticles as a Vaccine Platform: Influence of Size and Shape on Immunological Responses in Vitro and in Vivo. *ACS Nano* **2013**, *7* (5), 3926–3938. DOI: 10.1021/nn3057005.

(33) Kampert, T.; Misra, S. K.; Srivastava, I.; Tripathi, I.; Pan, D. Phenotypically Screened Carbon Nanoparticles for Enhanced Combinatorial Therapy in Triple Negative Breast Cancer. *Cellular and Molecular Bioengineering* **2017**, *10* (5), 371–386. DOI: 10.1007/s12195-017-0490-y.

(34) Aitken, C. E.; Marshall, R. A.; Puglisi, J. D. An Oxygen Scavenging System for Improvement of Dye Stability in Single-Molecule Fluorescence Experiments. *Biophysical Journal* **2008**, *94* (5), 1826–1835. DOI: 10.1529/biophysj.107.117689.

(35) Zheng, Q.; Jockusch, S.; Zhou, Z.; Blanchard, S. C. The Contribution of Reactive Oxygen Species to the Photobleaching of Organic Fluorophores. *Photochemistry and Photobiology* **2014**, *90* (2), 448–454. DOI: 10.1111/php.12204.

(36) Alander, J. T.; Kaartinen, I.; Laakso, A.; Pätilä, T.; Spillmann, T.; Tuchin, V. V.; Venermo, M.; Välisuo, P. A Review of Indocyanine Green Fluorescent Imaging in Surgery. *International Journal of Biomedical Imaging* **2012**, *2012*, 1–26. DOI: 10.1155/2012/940585.

(37) Gomez, E.; Kodisana, M.; Harun, A.; Kornegay, A.; Hanson, K. K.; Srivastava, I.; Usama, S. M. Unsymmetrical heptamethine cyanines prevent aggregation. 2026, SPIE: p 5. DOI: 10.1117/12.3087306.

(38) Yoon, H. K.; Ray, A.; Koo Lee, Y.-E.; Kim, G.; Wang, X.; Kopelman, R. Polymer–protein hydrogel nanomatrix for stabilization of indocyanine green towards targeted fluorescence and

photoacoustic bio-imaging. *Journal of Materials Chemistry B* **2013**, *1* (41), 5611. DOI: 10.1039/c3tb21060j.

(39) Lee, Y.-H.; Lai, Y.-H. Synthesis, Characterization, and Biological Evaluation of Anti-HER2 Indocyanine Green-Encapsulated PEG-Coated PLGA Nanoparticles for Targeted Phototherapy of Breast Cancer Cells. *PLOS ONE* **2016**, *11* (12), e0168192. DOI: 10.1371/journal.pone.0168192.

(40) Yeroslavsky, G.; Umezawa, M.; Okubo, K.; Nigoghossian, K.; Thi Kim Dung, D.; Miyata, K.; Kamimura, M.; Soga, K. Stabilization of indocyanine green dye in polymeric micelles for NIR-II fluorescence imaging and cancer treatment. *Biomaterials Science* **2020**, *8* (8), 2245–2254. DOI: 10.1039/c9bm02010a.

(41) Kirchherr, A.-K.; Briel, A.; Mäder, K. Stabilization of Indocyanine Green by Encapsulation within Micellar Systems. *Molecular Pharmaceutics* **2009**, *6* (2), 480–491. DOI: 10.1021/mp8001649.

(42) Acs, M.; Babucke, M.; Jusufi, M.; Kaposztas, Z.; Slowik, P.; Hornung, M.; Schlitt, H. J.; Panczel, I.; Hevesi, J.; Herzberg, J.; et al. Current clinical practices of cytoreductive surgery (CRS) and hyperthermic intraperitoneal chemotherapy (HIPEC). *Innovative Surgical Sciences* **2024**, *9* (1), 3–15. DOI: 10.1515/iss-2023-0055.

(43) Gao, N.; Bozeman, E. N.; Qian, W.; Wang, L.; Chen, H.; Lipowska, M.; Staley, C. A.; Wang, Y. A.; Mao, H.; Yang, L. Tumor Penetrating Theranostic Nanoparticles for Enhancement of Targeted and Image-guided Drug Delivery into Peritoneal Tumors following Intraperitoneal Delivery. *Theranostics* **2017**, *7* (6), 1689–1704. DOI: 10.7150/thno.18125.

(44) Caruso, D.; Sammartino, P.; Polici, M.; Masci, G.; Biacchi, D.; Zerunian, M.; Scuto, D.; Gallotti, M. G.; Iafrate, F.; Laghi, A. Imaging of Peritoneal Surface Malignancies. *Journal of Surgical Oncology* **2024**, *130* (6), 1203–1212. DOI: 10.1002/jso.27979.

(45) Cortés-Guiral, D.; Hübner, M.; Alyami, M.; Bhatt, A.; Ceelen, W.; Glehen, O.; Lordick, F.; Ramsay, R.; Sgarbura, O.; Van Der Speeten, K.; et al. Primary and metastatic peritoneal surface malignancies. *Nature Reviews Disease Primers* **2021**, *7* (1). DOI: 10.1038/s41572-021-00326-6.

(46) Yan, H.; Feng, Y.; Jia, Q.; Zhang, R.; Wang, Z. Redox-Programmed Activation of a Dual-Modal Probe for High-Fidelity Tumor Delineation and Image-Guided Surgery. *Advanced Science* **2026**, *13* (16). DOI: 10.1002/advs.202519223.

(47) Alvero, A. B.; Kim, D.; Lima, E.; Sumi, N. J.; Lee, J. S.; Cardenas, C.; Pitruzzello, M.; Silasi, D.-A.; Buza, N.; Fahmy, T.; et al. Novel approach for the detection of intraperitoneal micrometastasis using an ovarian cancer mouse model. *Scientific Reports* **2017**, *7* (1), 40989. DOI: 10.1038/srep40989.

(48) Colby, A. H.; Berry, S. M.; Moran, A. M.; Pasion, K. A.; Liu, R.; Colson, Y. L.; Ruiz-Opazo, N.; Grinstaff, M. W.; Herrera, V. L. M. Highly Specific and Sensitive Fluorescent Nanoprobes for Image-Guided Resection of Sub-Millimeter Peritoneal Tumors. *ACS Nano* **2017**, *11* (2), 1466–1477. DOI: 10.1021/acsnano.6b06777.